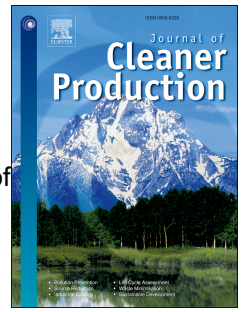

Fe^{3+} @ ZnO/polyester based solar photocatalytic membrane reactor for abatement of RB5 dye

Ambreen Ashar, Ijaz Ahmad Bhatti, Munir Ashraf, Asif Ali Tahir, Humera Aziz, Maryam Yousuf, Muhammad Ahmad, Muhammad Mohsin, Zeeshan Ahmad Bhutta

PII: S0959-6526(19)33880-6

DOI: https://doi.org/10.1016/j.jclepro.2019.119010

Reference: JCLP 119010

To appear in: *Journal of Cleaner Production*

Received Date: 2 August 2019

Revised Date: 7 October 2019

Accepted Date: 21 October 2019

Please cite this article as: Ashar A, Bhatti IA, Ashraf M, Tahir AA, Aziz H, Yousuf M, Ahmad M, Mohsin M, Bhutta ZA, Fe^{3+} @ ZnO/polyester based solar photocatalytic membrane reactor for abatement of RB5 dye, *Journal of Cleaner Production* (2019), doi: https://doi.org/10.1016/j.jclepro.2019.119010.

Fe^{3+} @ ZnO/POLYESTER BASED SOLAR PHOTOCATALYTIC MEMBRANE REACTOR FOR ABATEMENT OF RB5 DYE

Ambreen Ashar[1,2], Ijaz Ahmad Bhatti[1], Munir Ashraf*[3], Asif Ali Tahir[4], Humera Aziz[5], Maryam Yousuf[1], Muhammad Ahmad[6], Muhammad Mohsin[1], Zeeshan Ahmad Bhutta[7]

[1]Department of Chemistry, University of Agriculture, Faisalabad-38040, Pakistan
[1]Department of Chemistry, Government College Women University, Faisalabad, 38040, Pakistan
[3]Functional Textiles Research Group, National Textile University, Faisalabad-37610, Pakistan
[4]Energy and sustainability institute, University of Exeter, Penryn Campus, UK 9FE.TR10.
[5]Institute of Soil and Environmental Sciences, University of Agriculture, Faisalabad, Pakistan
[6]Department of Structure and Environmental Engineering, University of Agriculture, Faisalabad-38040, Pakistan
[7]Department of Clinical Medicine and Surgery, University of Agriculture Faisalabad-38040, Pakistan

*Corresponding Author: munir.ashraf01@gmail.com

Fe^{3+} @ ZnO/POLYESTER BASED SOLAR PHOTOCATALYTIC MEMBRANE REACTOR FOR ABATEMENT OF RB5 DYE

Abstract

Heterogeneous photocatalysis, employing semiconductor metal oxides, especially at nano scale is a promising technique to mortify the dye residues from effluent. The photocatalysts on doping with a suitable dopant can be modified to enhance the photocatalytic activity. In this study, undoped and series of Fe^{3+} doped ZnO has been grown on polyester fabric through low temperature hydrothermal method to generate photocatalytic membrane reactors (PMRs). The material grown on the surface of fabric was characterized by XRD, EDX, SEM, TEM, STEM, AFM, XPS, ICP-MS, DRS and PL studies. For ZnO/PMR and Fe^{3+}@ZnO/PMR photocatalytic activity was determined and examined to increase for Fe^{3+}@ZnO/PMR in the solar region due to the reduction of band gap from 3.2 to 2.6 eV on Fe^{3+}doping. The surface properties of PMRs were also determined by zeta potential and contact angle. The characterized ZnO and Fe^{3+}@ZnO nano discs based PMRs have been used to degrade RB5 reactive dye on irradiating with artificial sunlight (D65, 72 watts). The reaction parameters i.e. initial dye and oxidant concentration, pH and irradiation time have been optimized by Response surface methodology (RSM). The extent of dye degradation has been evaluated by UV/vis spectroscopy and FTIR. The maximum degradation achieved was 88.89 % for ZnO/ PMR and 98.34% for Fe^{3+}@ZnO PMR in 180 min. The photocatalytic efficiency of Fe^{3+}@ZnO PMR was investigated for 15 batches, with a slight gradual decrease in activity after eight batches.

Key words: functionalized polyester, photocatalytic membrane reactor, response surface methodology, Fe^{3+} @ZnO nanodiscs

Graphical Abstract

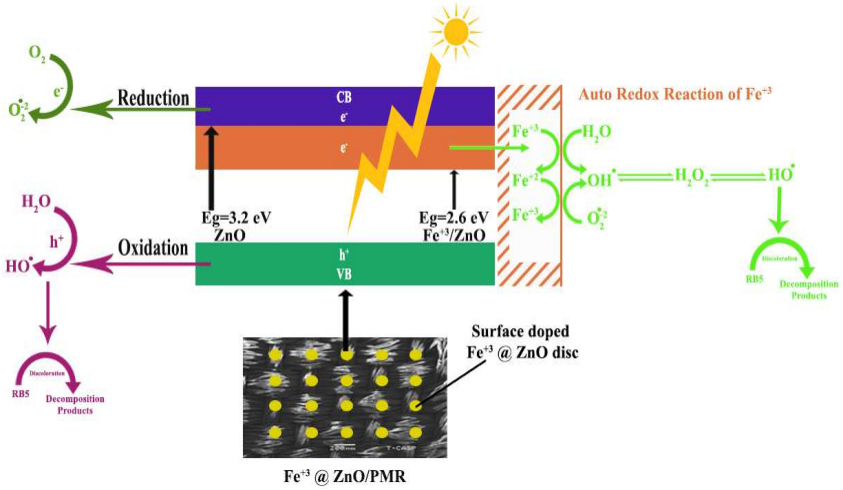

Introduction

In a modern society, massive production and use of dyes has led to the generation and dumping of aqueous effluents containing 20% of dye contents(Kaur et al., 2016).The metabolites produced after the incomplete biodegradation of recalcitrant dyes are not only carcinogenic and mutagenic but also retard the photosynthetic activity of aquatic flora (Sarkar et al., 2012; Yu et al., 2017; Zhang et al., 2012).The azo dyes, characterized by having an azo group (-N=N-), are the largest class of dyes considered as persistent organic pollutants (POPs) of textile effluents (Bello et al., 2017; Kansal et al., 2007).All conventional protocols for the treatment of wastewater are categorized as physical, chemical and biological processes that have limitations regarding their execution and efficiency. The heterogeneous photocatalysis employing semiconductor metal oxides has been proved to have remarkable advantages such as mineralization of broad spectrum of pollutants even at ambient temperature and pressure(Asghar et al., 2015; Chow et al., 2017; Giannakis et al., 2017; Kannangara et al., 2018; Prieto-Rodriguez et al., 2012; Thompson and Yates, 2006; Zheng et al., 2017).

Semiconductor metal oxides like ZnO, are of great importance as efficient in-situ generation of hydroxyl free radical on irradiation at neutral pH and can be utilized for the degradation of organic pollutants(Alaraby et al., 2015; Zheng et al., 2007). Nanostructures of ZnO are considered as the most competent candidate for wastewater treatment(Kołodziejczak-Radzimska and Jesionowski, 2014).The photocatalytic activity (PCA) of metal oxides greatly depends on morphology, surface area and bandgap (Long et al., 2017; Park et al., 2013).Doping of metal oxides with cations and/or anions increase the surface defects, decrease band gap and enhance PCA(Iqbal et al., 2014; Li et al., 2018; Park et al., 2009;

Zheng et al., 2009). Over the years, various methods have been adapted for the synthesis of one dimensional nanostructures of ZnO such as nanowires, nanobelts, nanorods, and nanowhiskers(Ashar et al., 2016; Tabata et al., 2010). It is evident through literature that still a little attention has been given to the synthesis of two dimensional (2D) structures.The specific fabrication methods in aqueous medium i.e. hydrothermal, precipitation and microemulsion processes enable to obtain 2D structures of ZnO with tunable size, shape and spatial properties(Sun et al., 2016).

Although powdered photocatalyst is being extensively employed for photocatalysis, yet its recovery from a slurry reactor is cumbersome to reuse (Chong et al., 2010).To overcome this predicament, it can be adhered to any substrate and fabric is particularly useful for this purpose based on the highest surface area, porosity and chemical resistance. The functionalized fabric can be efficiently used for effluent treatment but still just a few attempts have been made to generate photocatalytic membrane reactors (PMRs). The multifunctional textiles bearing special properties have been developed, like polyester grown ZnO nano rods are being used as antibacterial textiles in addition to self-cleaning and ultraviolet shielding etc.(Ashar et al., 2016; Jeong et al., 2014; Park et al., 2016).

Since only 4-5% of the incident solar radiation can be harvested by intrinsic ZnO, therefore, to improve light harvesting in solar range modification of ZnO photocatalyst is the most recent topic in the field of photocatalysis (Han et al., 2009; Sarkar et al., 2012; Shinde et al., 2015).The solar-driven photocatalysis has been proved to be a promising technique for remediation of POPs. Various configurations of photocatalytic membrane reactors (PMRs) involve the irradiation source fixed above the photocatalyst incorporated onto the surface of the membrane permanently in contact with effluent to be treated (Mozia et al., 2014). The prominent advantages of PMRs are their self-antifouling properties, high permeate fluxes, self-cleaning *via* light, reduced space requirements in addition to simultaneous filtration and photocatalysis (Molinari et al., 2017).

The present study involves the growth of 2D, intrinsic and surface doped Fe^{3+}@ ZnO on polyester fabric by low temperature hydrothermal method to be used as ZnO /PMR andFe^{3+}@ ZnO /PMR in artificial solar photocatalytic reactor to degrade CI Reactive Black 5 (RB5) bisazo dye as a probe. The dopant Fe^{3+} aided the redox reaction at the surface of photocatalyst support, enhancing the PCA due to band gap reduction causing improvement in harvesting the solar radiation. The role of Polyester as a substrate was to cause the magnificent retardation in agglomeration of photocatalyst in addition to the convenience in the reuse of PMR. The role of surface properties in enhancement of PCA has also been

investigated. The higher PCA of Fe^{3+}@ ZnO /PMR lead to accelerate the rate of photodegradation of bisazo RB5 dye for multiple batches of dye containing effluent without any substantial decrease in efficiency.

2. EXPERIMENTAL

2.1 Functionalization of polyester fabric with series of Fe^{3+}@ ZnO

To develop PMR, the functionalization of polyester fabric with nano-ZnO was done after depositing seed layer according to seeding method (Ashraf et al., 2013). For instance, polyester fabric was pretreated with 2M NaOH for 2 hours at 60 °C to generate polar groups on the surface. The seed solution of ZnO was prepared by refluxing 90 mM methanolic $Zn(CH_3COO)_2.2H_2O$ and 75 mM methanolic NaOH at 60 °C for 3 hours. The pretreated fabric was dipped in seed solution and squeezed between two rolls of padding machine to remove excess of liquor, and finally dried at 120 °C for 2 minutes. This process was repeated 10 times to ensure uniform deposition of seed layer on the fabric.

To grow nano-ZnO on seeded polyester, 0.2 M $Zn(SO_4)_{2.}7H_2O$ and0.4 M NaOH solutions were prepared using ultrapure water and mixed together while stirring at 200 rpm. Then, equal volume of reaction mixture along with 20x20 cm^2 pieces of seeded polyester fabric were shifted to six hydrothermal steel jars. The jars were screw capped and subjected to stirring at 90 °C in a laundrometer (TC-M-25). After 1 h, 2-10 wt% of $Fe(NO_3)_{3.}9H_2O$ solutions were added to five jars in the ratio of 5% V/V. The contents of one jar were left unaltered to get intrinsic ZnO. All the six jars were subjected to further stirring at 90 °C for another hour. After cooling the jars, pieces of polyester were spread for drying. Finally the excess of powdered intrinsic and doped ZnO was collected from the surface of polyester and all of the samples were preserved for characterization and determination of their PCA.

2.2. Photocatalytic degradation of dye

Photocatalysis has been carried out in borosilicate glass containers of 20x20x4 cm^3 containing 100 ml of RB5 dye solution for each experiment. Light intensity was kept constant at 72 watts using D65 cool artificial day light tubes fixed in a closed reactor at laboratory scale at 30-35 °C with 60 µg as an average catalyst load on 5 cm^2 swatch of PMR. The simple schematic diagram of solar photocatalytic reactor is as shown in Figure 1.

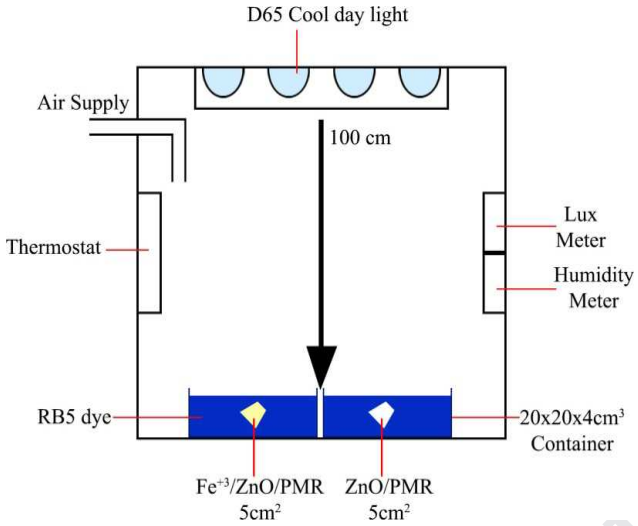

Fig.1. Schematic diagram of self-constructed solar photocatalytic reactor for degradation of RB5 using Fe^{3+}@ ZnO/PMR and ZnO/PMR

To optimize the reaction parameters the effects of sunlight irradiation time, pH, dye concentration and supporting oxidant on photocatalytic degradation, Response Surface Methodology (RSM) has been conceded out for investigating the independent and interactive effect of reaction parameters by varying them simultaneously in a limited number of experiments for optimization modeling. RSM applied under central composite design (CCD) has been effectively employed to optimize the photo-degradation of numerous organics (Ahamd et al., 2017). The statistical tool Design Expert 7 explained the effect of variables by suggesting 30 runs, which were performed to find out the percentage degradation of RB5 as a response. The interactive effects among the individual parameters were examined to find out the combination of their levels in order to optimize the conditions of the degradation process more accurately (Yücel and Yücel, 2015). Names of factors and their codes and levels are given in Table 1. The levels for operational parameters have been selected on the basis of previous investigations, especially the pH levels of the reaction mixture (Kazeminezhad and Azar Sadollahkhani., 2018). Response in photocatalytic experiments was % degradation of dye RB5 which is calculated using equation (1).

$$\text{Degradation } (\%) = \frac{A_o - A_f}{A_0} \times 100 \qquad \text{Equation (1)}$$

Where, $\mathbf{A_o}$: Initial absorbance of dye and $\mathbf{A_f}$**:** Absorbance of dye after photocatalytic treatment. A model prescribed by Design Expert 7 provided the individual and interactive effect of different parameters on % degradation of RB5.

Table 1: Coded reaction variables and their ranges investigated for optimization

Factor	Variables	Units	Low Actual	High Actual
X_1	pH	-	5	9
X_2	Oxidant Concentration (H_2O_2)	mM	10	50
X_3	Initial Dye Concentration	ppm	10	50
X_4	Sunlight	Hour (h)	1	5

3. Results and Discussion

3.1. Crystalline properties of fabricated material

The crystalline nature and variation in lattice parameters in intrinsic and series of Fe^{3+}doped ZnO have been determined by powder XRD. Figure 2 presents comparative diffractogram of nano-ZnO before and after doping with different levels of wt% of Fe^{3+} as dopant. The peaks appearing in diffractogram are indexed to JCPDS card No. 36-1451 which indicated all the prominent peaks of ZnO i.e. (100), (002) and (101). The hexagonal Wurtzite crystal system of ZnO is thus confirmed for the whole series of Fe^{3+}@ ZnO samples. The stress developed in the ZnO crystal due to surface doping caused shifting of peaks at slightly smaller 2θ with increasing level of wt% of Fe^{3+}dopant. The present results are in accordance with previously reported research (Karmakar et al., 2007; Shi et al., 2008; Chen et al., 2008).The shifting of peaks can be attributed to the difference in ionic radii of Fe^{3+} (0.067 nm) and Zn^{2+}(0.083 nm) ions (Srivastava et al., 2009). Conclusively, the lattice parameters of Fe^{3+}@ ZnO were slightly lesser than those of intrinsic ZnO, confirming that the Fe^{3+} ions have been substituted into the ZnO crystal lattice without altering the wurtzite structure (Cong et al., 2006). The appearance of no extra peak in diffractograms shows the purity of material except for the sample containing 1.00 wt. % of Fe^{3+} dopant. The higher concentration of Fe^{3+}caused the small extra peaks appearing at2θ=32·239° and 35.234°. The peak broadening for crystals of intrinsic and series ofFe^{3+}doped ZnO indicated that the crystallinity of ZnO has been declined by surface doping of ZnO with Fe^{3+} due to defect creation. The similar trend has been observed in previous researches on Fe^{3+} doping of ZnO (Ba-Abbad et al., 2013).

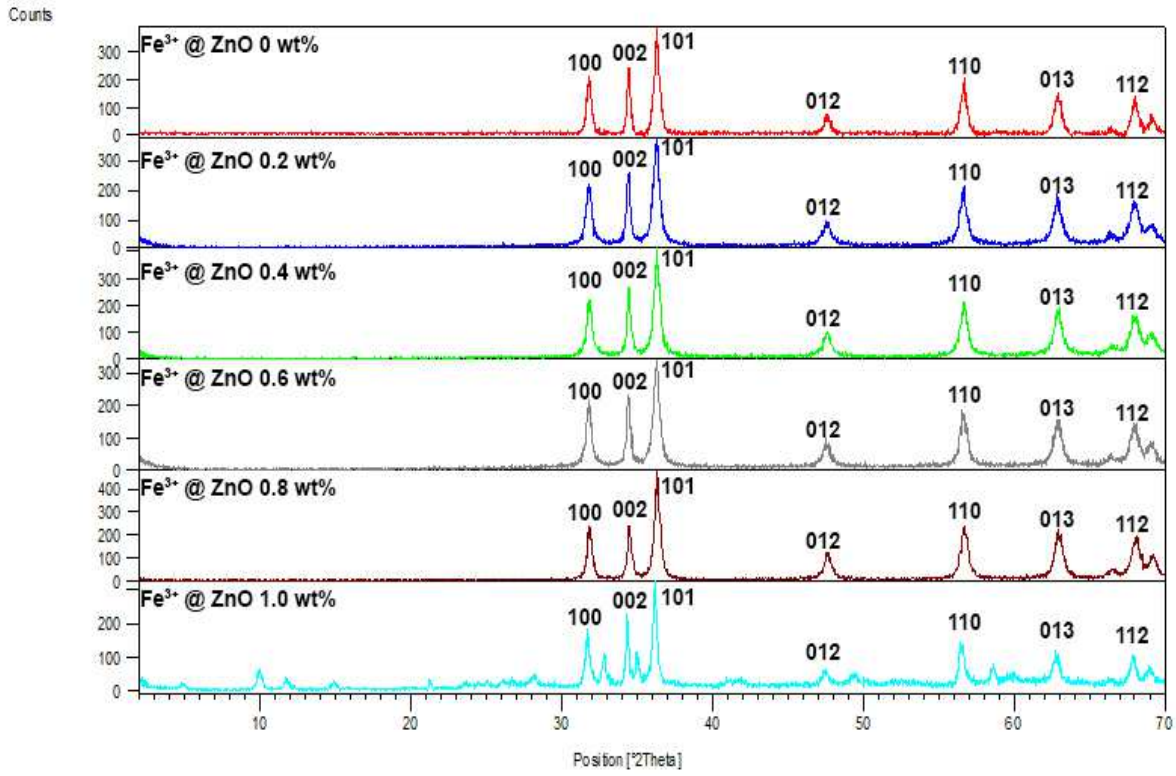

Fig.2. Comparative diffractograms of series Fe^{3+} @ ZnO samples collected from the surface of PMRs

The peak positions, FWHM, crystallite size calculated using Scherrer's formula and lattice parameters for the series of Fe^{3+} @ ZnO samples have been given in Table 2. The calculated crystallite size for intrinsic ZnO was 28.35nmand for 0.6wt%Fe^{3+}@ ZnO was 21.34 nm. Lattice constants of undoped ZnO are a= 3.25340 Å c= 5.20730 Å while aspect ratio c/a is 1.600. On doping with 0.6 wt % Fe^{3+} the lattice constants change to a= 3.24937 Å c= 5.20470 Å while c/a ratio turned 1.602. The increase in aspect ratio indicated about the fabrication of 2D nanostructures with decreasing thickness grown on the surface of polyester. The decrease in lattice constants and crystallite size is a strong evidence of defects created in a crystal of ZnO due to substitution of Zn^{+2} with Fe^{3+}.The results previously reported also showed that peak at (002) shifted towards smaller angle direction with that of Fe^{3+} and Fe^{2+} doping (Wang et al., 2008). On the basis of the most suitable crystalline properties the fabric sample with 0.6wt%Fe^{3+}@ ZnO was selected for further characterization in comparison to intrinsic ZnO.

3.2 Morphology of intrinsic and Fe^{3+}doped ZnO PMRs

Mono modal nano discs of intrinsic ZnO have been grown uniformly on the surface of every strand of polyester fabric to generate ZnO/PMR (Fig. 3a, b and c). Morphology of 0.6wt% of Fe^{3+}@ ZnO grown on the surface of polyester fabric was also discoid (Fig. 3d). It is evident from micrographs that upon surface doping of ZnO with Fe^{3+}, the particle size decreased from 93 nm to 72 nm and the surface was transformed owing to the development of kinks and corners on the surface (Fig. 3 d). This can be attributed to preferred growth of crystal in (100), a-axis while its retardation in (101), c-axis which became more prominent in the case of Fe^{3+}@ ZnO. It has also been described in previous studies that on Fe^{3+} doping the particle size decreased and surface roughness increased (Asiltürk *et al.*, 2009).

A group who worked on functionalization of polyester fiber has explained that on alkali treatment some scars and pores appeared on the surface of fibers as a result of surface etching. In other words, alkali treatment led to surface roughness of polyester fabric and these scars might have acted as the sites for penetration of nano particles (Becheri et al., 2008)

Morphological properties of intrinsic ZnO and Fe^{3+}@ ZnO discs were further explored by TEM. According to micrographs, thin two-dimensional discs having width of almost 100 nm has been synthesized, while length is beyond 100 nm (Fig.3e). The comparatively smoother surface of hexagons of crystalline intrinsic ZnO is quite visible. Mono-crystalline nature of intrinsic ZnO has been indicated by high resolution transmission electron microscopy (HRTEM) (Fig.3f). The continuous unidirectional lines are indicating crystal planes that having interplanner distance of 2.36 °A without any grain boundary. Mono-crystallinity of intrinsic ZnO has also been investigated through selected area electron diffraction pattern (SAED) which can be seen as dotted pattern, where each dot is indicating the specific plane i.e. (110), (101) and (011) (Fig.3g).

Morphological properties of Fe^{3+} @ ZnO illustrated by TEM has also shown the discoid structures with kinks and corners, visible along with thin coating of Fe^{3+} on the surface of ZnO (Fig.3h). The average particle size of the rectangular disc was 88×123 nm according to TEM Concurring reports also revealed through TEM and HRTEM study that the morphology is dependent on dopant content since it causes the reduction in c-axis lattice constant and change in the spacing between planes (Iqbal *et al.*, 2014). Poly-crystalline nature of Fe^{3+}@ ZnO has also been indicated by HRTEM (Fig.3i). The bi-directional crystal planes have appeared at a distance of 2.31 °A with large grain boundaries. Poly-crystallinity of Fe^{3+}@ ZnO has also been investigated through selected area electron diffraction pattern (SAED) which can be seen as continuous pattern (Fig.3j).

Previous researches have shown that the variation of the synthesis conditions significantly affects the surface properties of a photocatalyst The appearance of steps and kinks at previously flat surface of the semiconductors create active sites for redox reaction on photoexcitation (Koper and Klabunde, 1997).

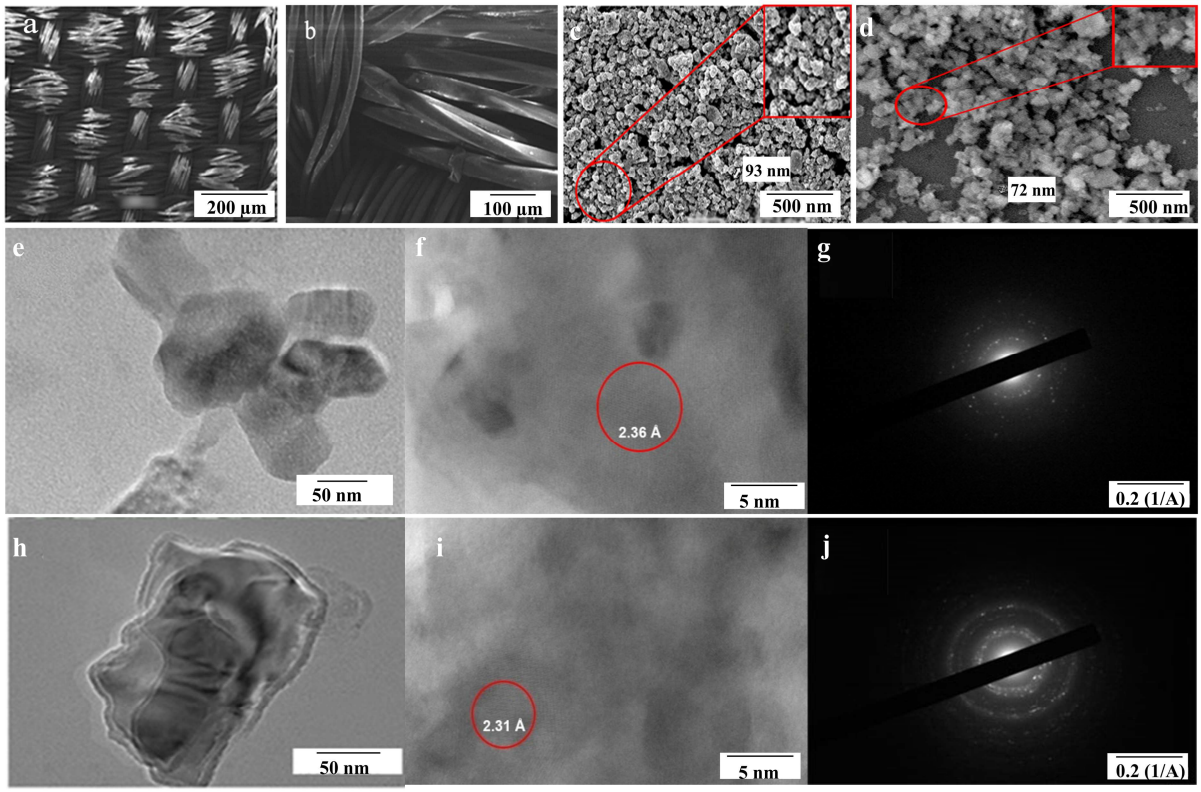

Fig.3. SEM images of a) Fe^{3+}@ ZnO discs grown on polyester at 2KX b) Magnified view of strands of polyester covered with Fe^{3+}@ ZnOdics at 25KX c). Pure ZnO nano-discs on a single strand of polyester 45KX d) Fe^{3+}@ ZnO nano-discs on a single strand of polyester at 45KX. TEM images of ZnO discs adhered to ZnO/PMR e) at 200 KX, f) HRTEM at 500KX g) SAED of ZnO discs .TEM images of Fe^{3+}@ ZnO discs h) at 200 KX, i) HRTEM at 500KX j) SAED of Fe^{3+}@ ZnO discs

The thickness of discs grown on Polyester has been determined by AFM and exhibited as 3D micrographs of tapping mode (Fig. 4 a,b). The maximum thickness of ZnO discs as given by tapping mode was 7 nm while that of Fe^{3+}@ ZnO discs was 5 nm. The enhanced roughness of Fe^{3+}@ ZnO discs is also evident from 3D view of tapping mode.This decrease in thickness of discs is concurrent with results of XRD and value of shape factor. The similar results were observed by other research groups (Iqbal *et al.*, 2014).

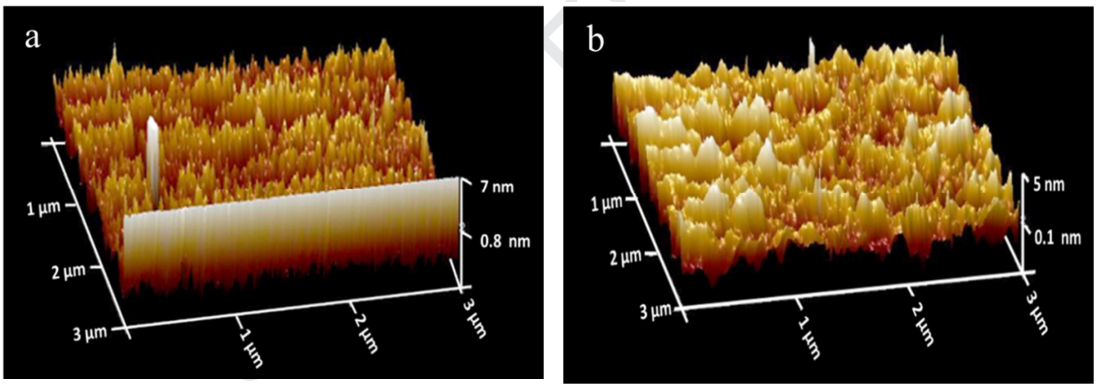

Fig.4. Tapping mode of AFM indicating thickness for a) ZnO discs b) Fe^{3+}@ ZnO discs

Both PMR have exhibited a significant roughness (Table S2) that obviously explains the strong adsorption abilities (Ahmad et al., 2017b). But this surface roughness significantly enhanced after doping with Fe^{3+} that is evident from values of skewness (sk) and kurtosis parameters, these parameters give an idea about symmetry of the surface. Generally, if there is symmetry in height distribution S_{sk} is zero, while positive value of skewness indicates asymmetrical surface having more peaks as compared to valleys. On the contrary, skewness is negative if the surface is relatively planar and more valleys are present (Kannangara et al., 2018). More negative values of S_{sk} i.e.-0.1 & -0.4 for ZnO and Fe^{3+}@ ZnO respectively and smaller values of kurtosis indicated that Fe^{3+}@ ZnO contains more valleys than ZnO PMR,

hence providing more space for penetration and adsorption of pollutant RB5 that ultimately favors high degradation of dye by Fe^{3+}@ ZnO PMR as compared to ZnO PMR (Ahmad et al., 2017a). Furthermore, average roughness (R_a) was calculated for both PMRs, $R_a$calculated for Fe^{3+}@ ZnO PMR was reduced (0.6 nm) as compared to ZnO PMR (1.1 nm) thus favoring increased surface roughness. Because decline in R_a values indicates that surface granules are becoming smaller leading to increment in surface area that increase adhesion followed by degradation of RB5 dye as compared to ZnO PMR. Conclusively, larger surface area, high surface roughness and more negative skewness values makes Fe^{3+}@ ZnO PMR more favorable catalyst as compared to ZnO PMR provided ideal surfaces for the rapid degradation of toxic RB5.

3.3. Elemental Composition of fabricated intrinsic ZnO and Fe^{3+}@ ZnO

The elemental detection for powdered ZnO obtained from the surface of ZnO /PMRand Fe^{3+}@ ZnO was executedthrough EDX. The spectrum (Fig. 5a) expressed the purity of the crystal and composition of zinc and oxygen in weight and atomic %. It can be observed that atomic % of oxygen is much higher than zinc, which can be correlated with the excess of adsorbed oxygen at the surface of crystal. Herein, the absence of any other element in the sample, assured its purity. On the other hand, EDX of Fe^{3+}@ ZnO has indicated that Zn is present in lower wt. % which shows that it has been substituted by some Fe^{3+} diffused in the crystal through the surface of the photocatalyst causing creation of defects. However, Zn is present in higher at. %, indicating that excess of Zn must be present at antisites. Moreover Fe^{3+} is present in traces i.e. 0.6% weight % and 0.45 atomic % as given in the graph (Fig. 5 b). In determining the PCA, atomic ratio of zinc to oxygen plays an important role regarding the number of active sites which depends upon presence of oxygen vacancies or zinc interstitials.

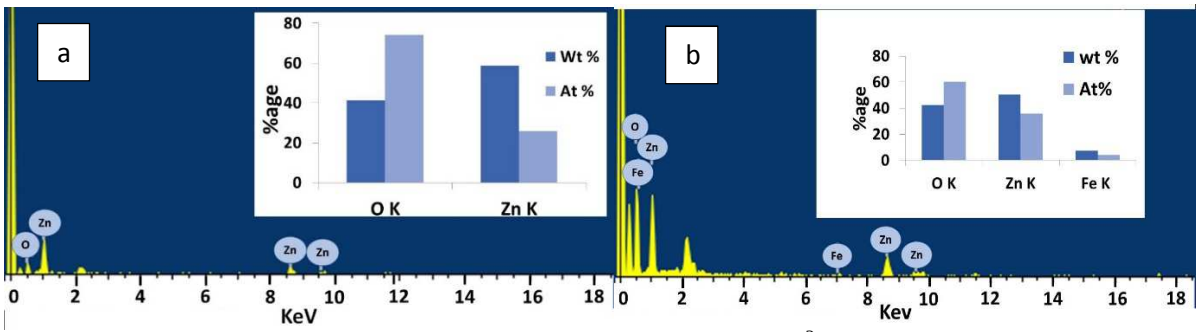

Fig.5. EDX of a) intrinsic ZnO discs obtained from ZnO/PMR b) Fe^{3+}@ZnO discs obtained from Fe^{3+}@ZnO/PMR

Surface elemental composition and doping has also been confirmed by STEM of intrinsic ZnO (Fig. S1 a,b) and Fe^{3+}@ ZnO . (Fig. S2 a,b,c). To determine the composition of metallic elements adhered to ZnO/ PMR and Fe^{3+}@ZnO/ PMR, ICP-MS was employed. According to the results amount of zinc found in intrinsic ZnO/PMR was 165.8 ppm. Whereas, the amount of zinc and iron concentration detected for Fe^{3+}@ZnO/PMR was 1.341 ppm and 0.034 ppm respectively.

Chemical composition and valence state of Fe in Fe@ZnO was determined using X-ray photoelectron spectroscopy (XPS).Carbon 1s core level peak (285.0 eV) was taken as the reference for calibrating (Moulder et al., 1992)and analyzing XPS spectra of Fe @ ZnO. Furthermore, percentage composition and atomic concentrations of Zn, O and Fe present in Fe @ ZnO calculated by measuring area under the peaks for respective elements. The survey spectrum of XPS of Fe@ZnO showed few carbon contents and no metallic impurity except Fe metal in ZnO lattice and confirmed the presence of Zn, O, and Feinvarying percentages in prepared Fe@ZnO.Strong peaks observed at binding energies in the range of 1020 eV-1050 eV are associated with Zn $2p_{3/2}$ and Zn $2p_{1/2}$ (Fig. 6). Further, Zn is present as Zn^{2+} state in prepared Fe@ZnO because observed binding energies of Zn are in strong agreement with the binding energy of 'Zn' present in ZnO lattice rather than elemental Zn (Lee et al., 2002; Srinivasulu et al., 2017). Due to oxygen atoms bonded to Zn in ZnO lattice core level XPS peak for O 1s was observed at 530.10 eV(Islam et al., 1996).

Peaks due to Fe $2p_{3/2}$ and Fe $2p_{1/2}$ duplet can be observed at binding energy of 710.5 and 724.0 eV. Binding energy difference is of 13.5 eV that arises due to spin–orbit coupling ruling out Fe-Fe clusters in Fe@ZnO that can be observed at 13.10 eV energy difference(Lee et al., 2008). Moreover, observed binding energy values are different from binding energies for elemental Fe and Fe present in FeO. Further, binding energy values obtained in our study are in close agreement to Fe^{3+} peaks corresponding to 710.70 eV of Fe $2p_{3/2}$ and 724.30 eV of Fe $2p_{1/2}$ reported in previous literature (Briggs, 1981; Karamat et al., 2014; Rambu et al., 2013). From XPS spectra it can be inferred that Fe in Fe@ZnO sample is present in Fe^{3+}valence state.

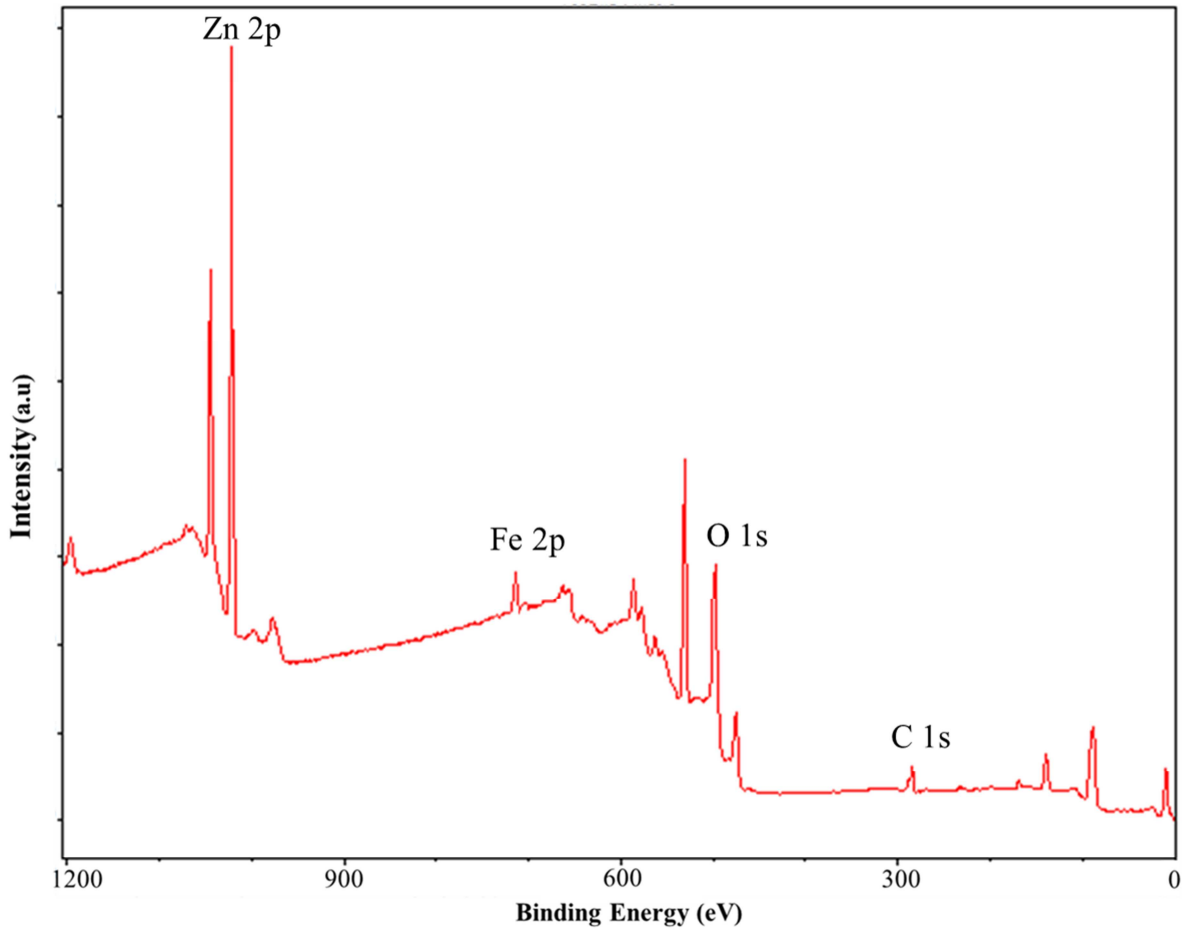

Fig.6. Survey spectrum of Fe^{3+}@ZnO for binding energy

3.4. Optical properties of intrinsic ZnO and Fe^{3+}@ZnO PMRs

The comparison of diffused reflectance of intrinsic ZnO and series of Fe^{3+} @ZnO has indicated that 85% of the sunlight is reflected by intrinsic ZnO, that is why, very minute photocatalytic activity is shown in solar range by colorless intrinsic ZnO. However, Fe^{3+} @ZnO absorbs 75-90 % of solar radiations in a whole range as given in diffused reflectance spectra of both photocatalysts (Fig. 7a).

Optical properties of fabricated materials have been examined through bandgap energies of intrinsic ZnO and Fe^{3+}@ ZnO . Bandgap energy for intrinsic and Fe^{3+}@ ZnOnano discs was calculated by using Kubelka-Munk plot using the data obtained by diffused reflectance spectroscopy (DRS)

The bandgap of intrinsic ZnO calculated by using Kubelka Munk plot was 3.2 eV(Fig.7b) , while bandgap calculated for Fe^{3+}@ZnO was 2.6 eV (Fig.7c), which shows the absorbance edge at 385nm falling in the visible range of solar spectrum. The decrease in bandgap can be

explained based on the fact that induction of Fe^{3+} on the surface of the ZnO crystal caused the creation of surface defects and inter-band energy states bellow the conduction band (CB). Consequently, electron requires lesser energy to get excited from valence band (VB) to (CB).

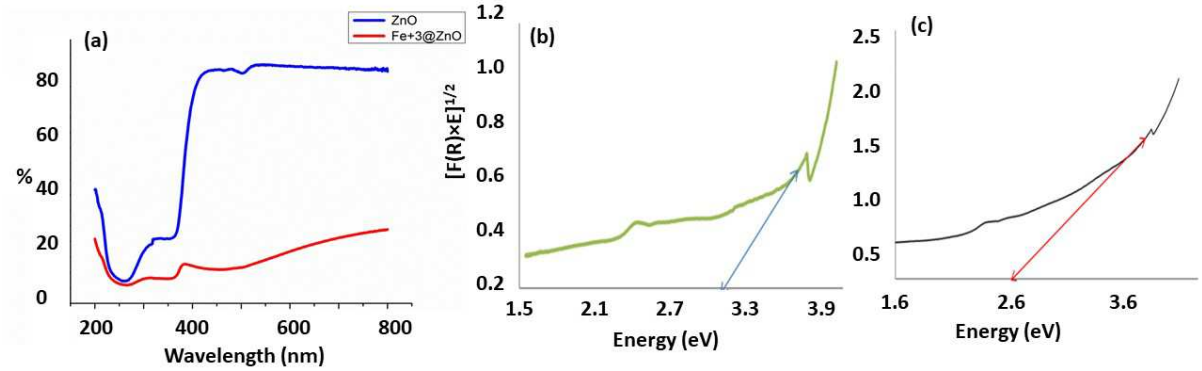

Fig.7a. Diffused reflectance spectrum for intrinsic ZnO and Fe^{3+}@ ZnO samples. Bandgap energy of b) undoped ZnO nano discs, c) Fe^{3+}@ZnO nano discs

The optical properties were further verified by photoluminescence study of the fabricated photocatalysts. The excitation and emission graphs of intrinsic ZnO and Fe^{3+}@ZnO can be seen in supplementary document (Fig.S3).

The hydrophilic nature of the surface of photocatalyst is indicative of high rate of diffusion and adsorption at its surface. In case of intrinsic ZnO PMR contact angle measured was 120° which indicated the low wettability of the surface of photocatalyst. On doping, the wettability increased significantly and the water droplet was almost spread over the surface in 7.5 second (complete data is available in supplementary document). The Coloumbic force of attraction between substrate (RB5) and heterogeneous photocatalyst is required to increase the rate of adsorption. As illustrated in graph of zeta potential the value for intrinsic ZnO lies mostly in negative region and the average value obtained was -3.64 mV under degradation conditions. This value changes to be positive (+7.46 mV) on doping. Detailed results are available in supplementary document.

3.5. Photocatalytic Activity of intrinsic ZnO and Fe^{3+}@ZnO

The fabricated intrinsic ZnO and Fe^{3+}@ZnO nano discs grown on polyester have been utilized for photodegradation of RB5 dye on exposure to artificial sunlight of fixed intensity (72 watts). The optimization of reaction parameters has been executed through Response surface Methodology (RSM). The main advantage regarding model suggestion is that experimental runs provided were less time consuming, cost-effective and more accurate for

optimization of variable parameter. As a response of 30 runs devised by software, % degradation was provided to optimize the independent and interactive reaction parameters.

The individual parameters optimized through experiments suggested as single factor effect by Design expert 7 were (X_1) pH =7, (X_2) H_2O_2 concentration=30 mM,(X_3), initial dye concentration =30 ppm and irradiation time (X_4) =3h. All of these parameters were found to have significant interactions among them. The interactive effects of operational parameters have been explained in Fig.15 in terms of 3D surface plots. Each plot displays variation in two parameters keeping the other two constant. Considering the interactive effects of initial dye concentration and pH on photodegradation response of RB5 indicated that maximum degradation of 88.89 % took place for 30 ppm of dye solution at pH 7, when H_2O_2 concentration was 30 mM and irradiation time was 3 hours , while it decreased with increase in dye concentration from 30 ppm to 50 ppm (Fig.8 a). According to 3D surface plot obtained for interaction between pH and H_2O_2 concentration, the maximum dye degradation of 85.84 % was examined when 30 mM of H_2O_2 was used as oxidant at pH 7 using 30ppm of dye solution and irradiating it under artificial sunlight for 3 hours. At the values of variables bellow and above these levels, the percentage degradation falls, while the interaction was significant (Fig. 8 b). According to surface plot of interactive effect of pH and irradiation time, at pH 7, on 3 hours of sunlight irradiation maximum degradation observed was 85.80 % when oxidant concentration was 30 mM and dye concentration was 30 ppm (Fig.8 c). The interactive effect of initial dye and H_2O_2 concentration indicated that greater concentration of dye require slightly higher concentration of oxidant H_2O_2. At PH 7, with the increase in oxidant concentration from 10 to 30 ppm % degradation of dye increased to 84.23% when 30 mM of oxidant was used for 30 ppm of dye solution (Fig. 8 d). Interactive effect of oxidant concentration and irradiation time, at 30 mmol of H_2O_2 concentration, 85.84 % degradation was noticed after 3 h of irradiation at pH 7 when dye concentration was 30 ppm under identical reaction conditions photodegradation % remained almost same (Fig.8 e). Interaction between initial dye concentration and irradiation time has been appeared as maximum degradation of 85.76 % taking place for 30ppm of solution when pH was set at 7 and H_2O_2 concentration was 30 mM and irradiation time was 3 hours (Fig, 8 f).

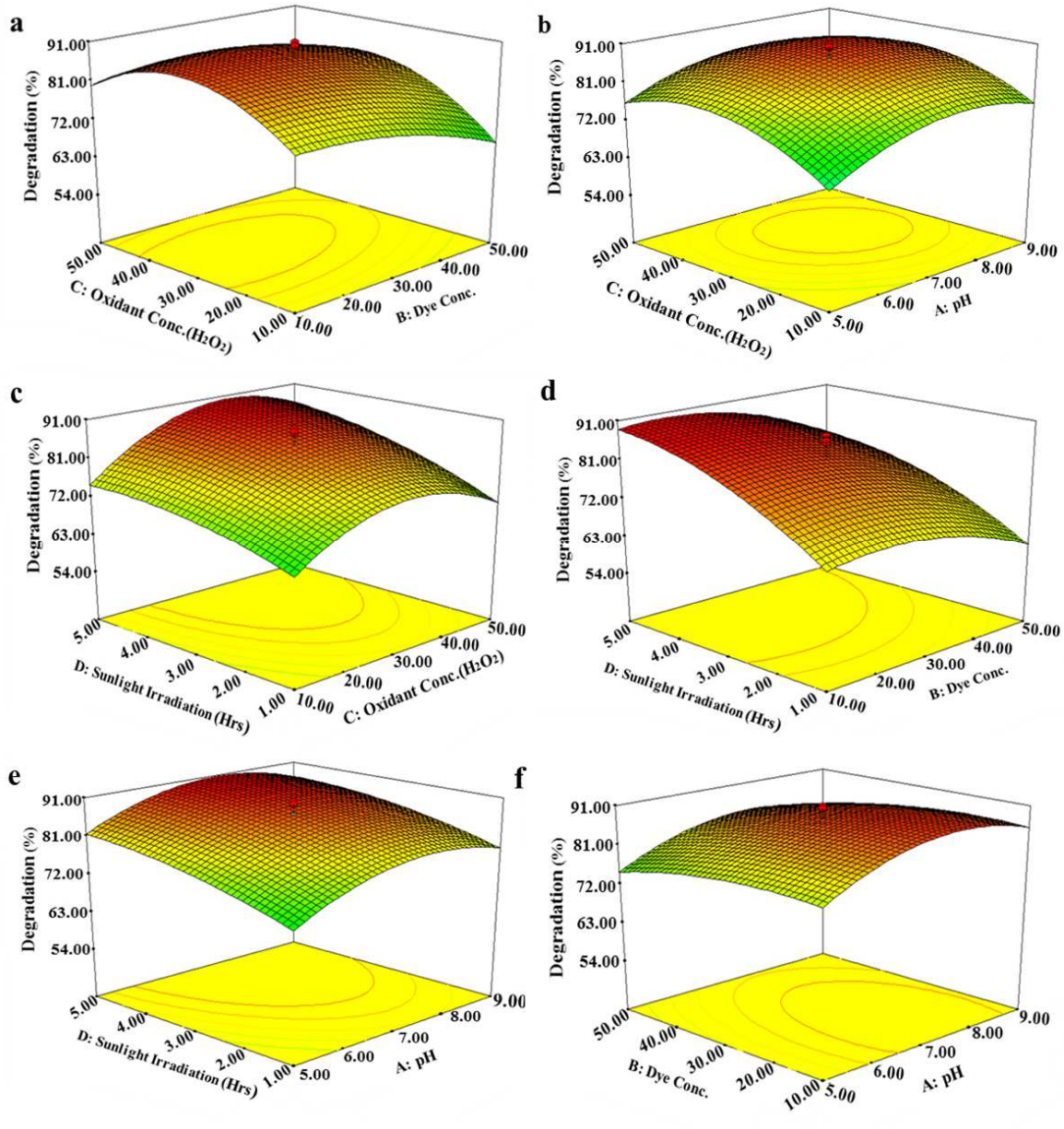

Fig.8.a) Interactive effect of initial concentration of dye and oxidant conc. b) Interactive effect of H_2O_2 and pH c) Interactive effect of sunlight irradiation time and H_2O_2 d) Interactive effect of initial concentration of dye and sunlight irradiation time. e) Interactive effect of sunlight irradiation time and pH f) Interactive effect of initial concentration of dye and pH

The rate of adsorption of each dye on the surface of photocatalyst is different at various pH. A report of previous study has explained that degradation of RB dye was faster in neutral and slightly alkaline medium (pH=8) while no adsorption took place at pH=11 (Kazeminezhad and Azar Sadollahkhani., 2018). In this study, the highest rate of degradation was achieved at pH 7 for RB5 because surface of ZnO at pH lesser than point of zero charge (Pzc) attain

positive charge. To attract anionic RB5 dye for adsorption prior to photocatalysis the positively charged surface acts as Lewis acid and allows dye molecule to behave as Lewis base, forming an intermediate complex.. Since pzc of ZnO is 9.5, pH 7 is as an optimum. pH for a redox reaction of anionic dye which enhanced the photocatalytic activity of ZnO/PMR for the degradation of RB5 (Fig 8 a, b, c).

Rate of photocatalytic degradation of RB5was accelerated with elevated H_2O_2concentration as it acts as an inhibitor of recombination and aided in the *insitu* generation of oxidizing agents $^{\bullet}OH$. Self-decomposition of H_2O_2 took placeon irradiation and due to reduction of H_2O_2 on trapping electron from conduction band (CB) results in increased concentration of $^{\bullet}OH$ in reaction mixture. Highest degradation of RB5 required 30 Mm H_2O_2 concentration while its dosage beyond the optimum level results in retarded rate of degradation. This effect is explainable on the basis of self-recombination of highly reactive $^{\bullet}OH$ radicals as an alternate and competitive reaction (fig 8 b, d, e,).

Initial concentration of pollutant dye has a crucial role in its degradation on the surface of heterogeneous photocatalyst. As the initial concentration of RB5 increased, rate of degradation also increased but exceeding the optimum concentration rate of degradation decreased. The reason behind it is that in low concentration of dye enough surface area is available for adsorption resulting in the ultimate high rate of degradation. Contrarily, when the concentration of dye is higher than optimum level, sufficient surface area for adsorption becomes unavailable. Following the Langmuir's theory of adsorption, rate of degradation of dye was declined. That is why, when the concentration of dye increased from 10 till 30 ppm, rate of degradation also increased but on further increase in concentration, the rate of degradation rate decreased. The other important factor causing the retarded rate of degradation was the blockage of sunlight due to highly colored reaction mixture containing excess of dissolved dye. At a high dye concentration, a significant amount of light can be absorbed by the dye molecules rather than by the photocatalyst resulting in a decrease in the formation of $^{\bullet}OH$ and $^{\bullet}O_2^{-2}$ as well as the photocatalytic activity. The decrease in intensity of sunlight adversely effects the rate of generation of electron-hole pair (Fig.8.c, d, e) .

Since all the experiments were performed under artificial sunlight with irradiation time of 1 to 5 h. Results have declared that degradation of RB5 was increased with increase in irradiation time keeping the intensity of light constant. But after 3h there was no significant effect on rate of degradation of RB5 indicating that it has become constant (Fig.8.c,e,f). Conclusively it is justified that optimized conditions for degradation of 30 ppm of RB5 dye using Fe^{3+}@ ZnO/PMR are pH =7, H_2O_2concentration =30 mM and irradiation time 3 h.

Bis azo RB5 dye is anionic in nature with negatively charged surface in an aqueous solution while surface of Fe^{3+}@ ZnO is positive, thus opposite charges enhance the rate of adsorption and ultimately the efficiency of the photocatalyst(Kansal et al., 2007). In addition, a positively charged surface directs the migration of photo-induced electrons to increase the concentration of $^{\bullet}OH$. This process also inhibits recombination simultaneously generating more $^{\bullet}OH$ as a result of reaction of h^{+} with water (Hassan et al., 2017).Under the optimized reaction conditions % of degradation of RB5 increased to 98.34% for Fe^{3+}@ ZnO PMR in 180 min.

The high regression coefficient (R_2= 0.91, R_{adj} =0.83) between the variables and the response indicated excellent estimate of experimental data by quadratic mode with CV % = 7.22 and pure error< 0.0001In the model applied the low value of CV indicated that the model was exceedingly significant while lack of fit was non significant according to software.The ANOVA (Table S1) has been given in supplimentry.

3.6. Evaluation of extent of photodegradation of RB5 dye

The extent of decolorization of RB5 was compared on irradiating a swatch of ZnO/PMR and Fe^{3+}@ ZnO/PMR dipped in 30 ppm of dye solution using D65 light under optimized conditions, using 30 mM of H_2O_2 concentration at pH 7 for 3h (Fig. 9). Bisazo RB5 anionic dye has shown absorbance maximum at 600 nm. When C/C° (final concentration /Initial concentration of dye) values of untreated dye, oxidant and dye treated by ZnO/PMR and Fe^{3+}@ ZnO/PMR was plotted with respect to time. It became clear that untreated dye did not show any decrease in C/C° with respect to time, so was the case with H_2O_2, taken as control. On using ZnO/PMR, C/C° value decreased on irradiation with sunlight after 10 min of adsorption period, but degradation achieved was much lesser as compared to Fe^{3+}@ ZnO/PMR, which showed maximum degradation in 180 min (Fig.9).

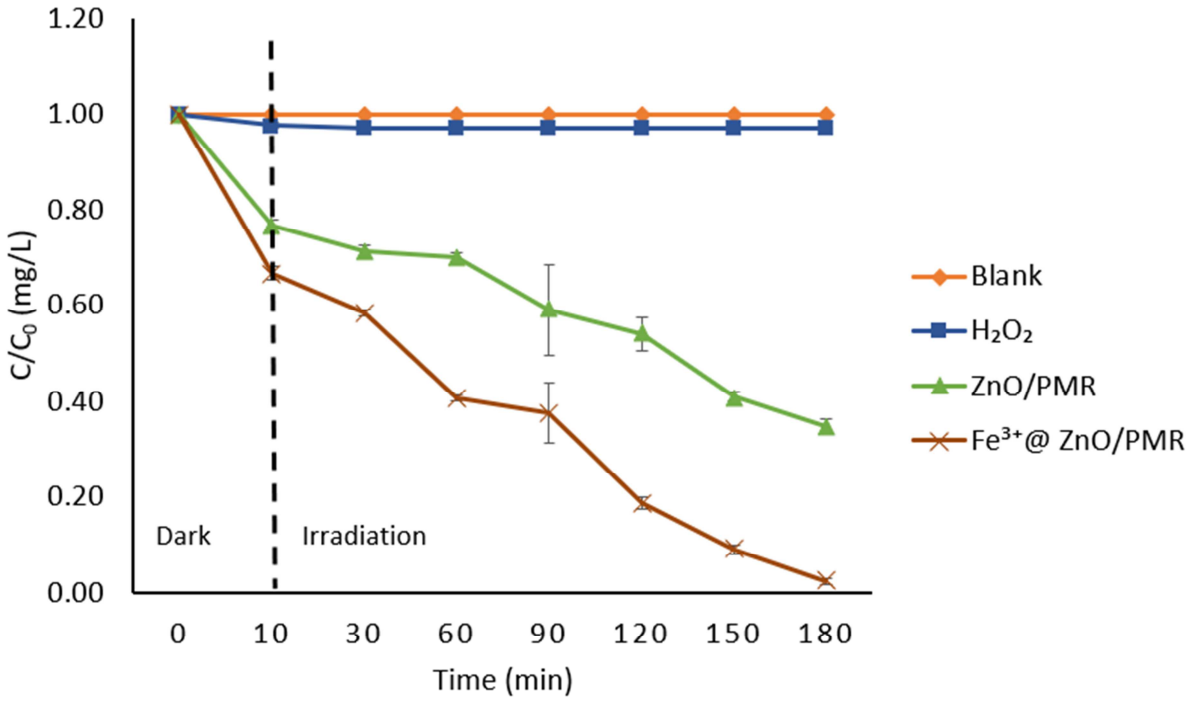

Fig.9. Determination of extent of photocatalytic degradation (C/C_0) of RB5 using ZnO/PMR and Fe^{3+}@ ZnO/PMR with respect to time.

Overlay UV/vis spectra for comparison of decolorization of dye by ZnO/PMR and Fe^{3+}@ ZnO/PMR indicated that the Fe^{3+} doping has remarkably enhanced decolorization of RB5, whereas UV/vis spectrum of H_2O_2 was taken as control. This is in accordance of previous studies that doping of ZnO with Fe^{3+} can reduce the band gap and conclusively increase the rate of generation of $^{\bullet}OH$. This fact can be attributed to the higher ability of and Fe^{3+}@ ZnO/PMR to harvest visible range of solar radiation enhancing its PCA. The other factors synergizing the PCA were higher surface roughness and hydrophilicity causing increase in rate of adsorption.

FTIR of untreated dye has shown a strong band at 3355.33 cm^{-1}due to N–H stretching and very small peak at 1114.35 $cm^{-1}$is due to C–N stretching and at 1480 cm^{-1}due to N=N azo group.The spectrum of treated dye is indicating that RB5 has been degraded to simpler hydrocarbons. The peak at 1480 cm^{-1} has almost vanished in treated dye. Moreover, the strong peak at 1616 cm^{-1} has shortened o great extent illustrating the loss of –NH group. Similarly peak near 750 cm^{-1} is the peak of benzene ring, which has also shortened in treated dye. A very small peak at 1541.45 cm^{-1} indicated C=C in aromatic ring. The peak at 3355.33 cm^{-1} also shortened to great extent indicating the loss of –NH group, no peak regarding the presence of aryl amines was found in the spectrum of treated RB5. . The spectral setup

observed was found similar to that reported in other photodegradation reports (Gahlout et al., 2013; Neoh et al., 2015).

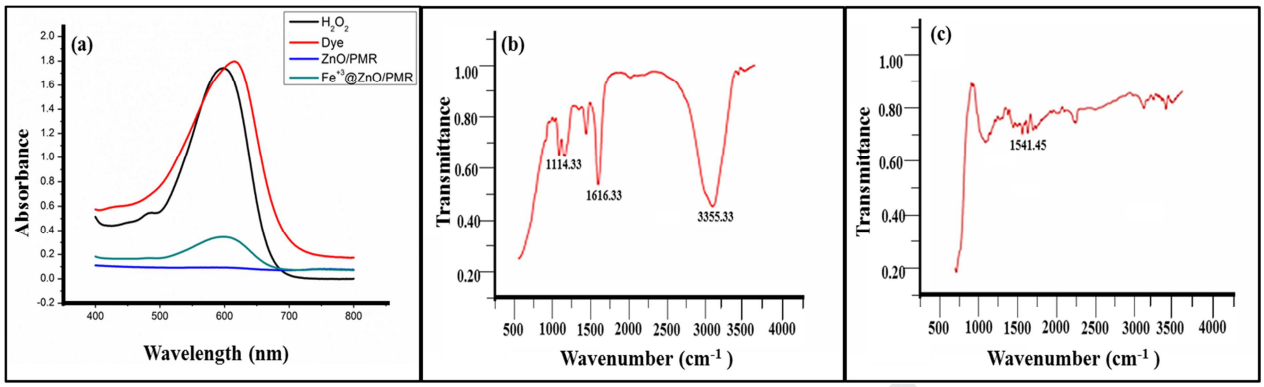

Fig.10.a) Comparison of extent of degradation of RB5 using ZnO/PMR and Fe^{3+}@ ZnO/PMR by UV/vis spectroscopy. FTIR Spectra of b) untreated and c) treated dye RB5

The faster rate of recombination of charge carriers subsequently decreases the amount of $^{\bullet}OH$ generated by the semiconductor and reduces the efficiency of the photocatalyst. Presence of crystalline defect can retard the rate of recombination by trapping charge carriers from the surface the semiconductor. Inside the volume of crystal, number of the trapping and recombination sites have to be reduced by synthesizing a photocatalysts with better crystallinity (Ângelo et al., 2013).

When nano discs of ZnO were doped with $Fe^{3+,}$ the optical properties changed based on the reduction of crystallite size and narrowing of band gap(Molinari et al., 2017). The PCA has been enhanced byFe^{3+} doping, based on the shuttling redox reaction between Fe^{3+} and Fe^{2+} (Fe^{3+} / Fe^{2+} redox couple). On capturing electron from conduction band of ZnO, more were the electrons produced causing appearance of Fe^{2+} from Fe^{3+}, more were $^{\bullet}OH$ radicals generated (Sahel et al., 2010).

3.7. Advantages and reusability of Fe^{3+}@ ZnO/PMR

Employment of Fe^{3+}@ ZnO/PMR for photocatalysis led to enhancement in the rate of degradation of RB5 due to non-agglomeration of nanomaterials adhered to substrate strongly. The porosity of substrate offered extensive surface area for adherence of Fe^{3+}@ ZnO (Zhang et al., 2012). In comparison to coatings seed mediated hydrothermal epitaxial growth has been found more long lasting (Ashraf *et al.*, 2013). Reuse of the catalyst in multiple cycles is convenient as removal of Fe^{3+}@ ZnO/PMR from reaction mixture does not require any

filtration or centrifugation. Washing of Fe^{3+}@ ZnO/PMR swatch after every cycle did not eroded Fe^{3+}@ ZnO even after15 batches and maintained its photocatalytic efficiency (Fig. 11). As given in the graph less than 10% of efficiency has been decreased after batch 8 gradually for each followed till batch 15. It can be accessed from given data that Fe^{3+}@ ZnO/PMR can be used further for multiple photocatalytic cycles. The reusability of the PMR offers a magnificent advantage as polyester is resistant to chemicals, moderately high temperature and sunlight.

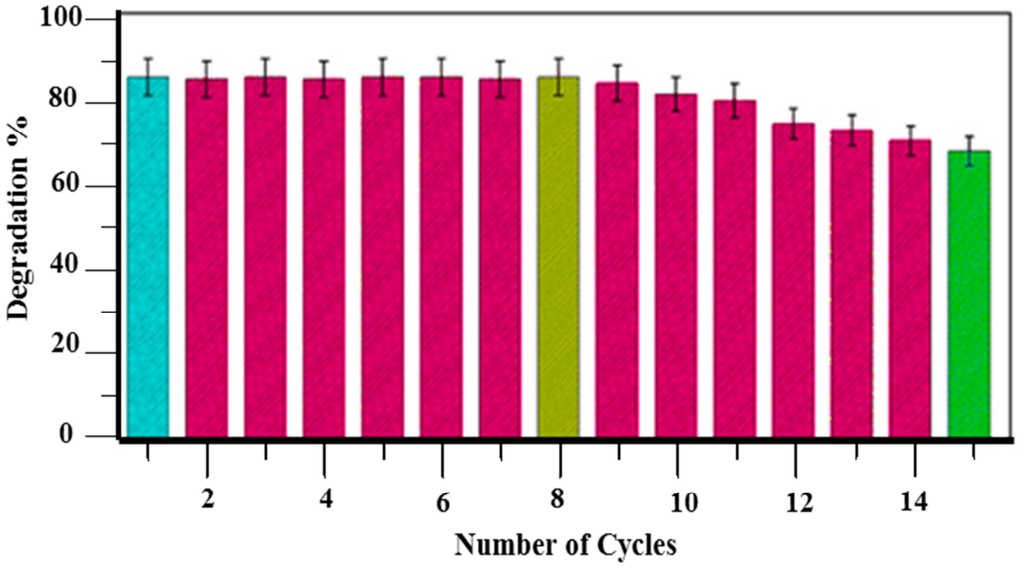

Fig.11. Reusability of Fe^{3+}@ ZnO/PMR

The rate constant (k) for average C/C_0 values obtained from batch experiments performed in triplets has been calculated as Pseudo first order reaction using the formula "$\ln(C_0/C)= kt$" (Molinari *et al.*, 2017).The rate constant calculated for First cycle was 14.28×10^{-3} min^{-1} and 12.28×10^{-3} min^{-1} for 15th cycle respectively (Table S2).

Conclusion

It can be concluded that Doping of ZnO with Fe^{3+}can lead to decrease in band gap to render it capable of harvesting high content of sunlight. Topography by SEM and TEM of the material synthesized have suggested 2Ddisc morphology with surface coating of Fe^{3+}. The material adhered to polyester decreased agglomeration of nano discs and thus Fe^{3+}@ ZnO/PMR acted as a novel solar active material reusable for photocatalytic treatment of dye RB5. Operational parameters of Photocatalysis have been optimized through RSM.Maximum degradation of

RB5 at pH7 using 30 mmol of H_2O_2 concentration for 30 ppm of dye was 88.89 % for ZnO/ PMR and 98.34% for Fe^{3+}@ZnO PMR in 180 minof irradiation with sunlight. Degradation products of RB5 dye consisted of simple hydrocarbons as indicated by FTIR and HPLC. The reusability of Fe^{3+}@ ZnO/PMR with almost similar efficiency was noticed on 15 washings and photocatalytic cycles.

Reference

Ahamd, M.Z., Ehtisham-ul-Haque, S., Nisar, N., Qureshi, K., Ghaffar, A., Abbas, M., Nisar, J., Iqbal, M., 2017. Detoxification of photo-catalytically treated 2-chlorophenol: optimization through response surface methodology. Water Sci. Technol. 76(2), 323-336.

Ahmad, M., Liu, S., Mahmood, N., Mahmood, A., Ali, M., Zheng, M., Ni, J., 2017a. Effects of porous carrier size on biofilm development, microbial distribution and nitrogen removal in microaerobic bioreactors. Bioresour. Technol. 234, 360-369.

Ahmad, M., Liu, S., Mahmood, N., Mahmood, A., Ali, M., Zheng, M., Ni, J., 2017b. Synergic Adsorption–Biodegradation by an Advanced Carrier for Enhanced Removal of High-Strength Nitrogen and Refractory Organics. ACS Appl. Mater. Interfaces 9(15), 13188-13200.

Alaraby, M., Annangi, B., Hernández, A., Creus, A., Marcos, R., 2015. A comprehensive study of the harmful effects of ZnO nanoparticles using Drosophila melanogaster as an in vivo model. J. Hazard. Mater. 296, 166-174.

Ângelo, J., Andrade, L., Madeira, L.M., Mendes, A., 2013. An overview of photocatalysis phenomena applied to NOx abatement. J. Environ. Manage. 129, 522-539.

Asghar, A., Raman, A.A.A., Daud, W.M.A.W., 2015. Advanced oxidation processes for in-situ production of hydrogen peroxide/hydroxyl radical for textile wastewater treatment: a review. J. Cleaner Prod. 87, 826-838.

Ashar, A., Iqbal, M., Bhatti, I.A., Ahmad, M.Z., Qureshi, K., Nisar, J., Bukhari, I.H., 2016. Synthesis, characterization and photocatalytic activity of ZnO flower and pseudo-sphere: Nonylphenol ethoxylate degradation under UV and solar irradiation. J. Alloys Compd. 678, 126-136.

Ashraf, M., Campagne, C., Perwuelz, A., Champagne, P., Leriche, A., Courtois, C., 2013. Development of superhydrophilic and superhydrophobic polyester fabric by growing zinc oxide nanorods. J. Colloid Interface Sci. 394, 545-553.

Asiltürk, M., Sayılkan, F., Arpaç, E., 2009. Effect of Fe3+ ion doping to TiO2 on the photocatalytic degradation of Malachite Green dye under UV and vis-irradiation. J. Photochem. Photobiol., A 203(1), 64-71.

Ba-Abbad, M.M., Kadhum, A.A.H., Mohamad, A.B., Takriff, M.S., Sopian, K., 2013. Visible light photocatalytic activity of Fe3+-doped ZnO nanoparticle prepared via sol–gel technique. Chemosphere 91(11), 1604-1611.

Bello, M.M., Raman, A.A.A., Purushothaman, M., 2017. Applications of fluidized bed reactors in wastewater treatment–a review of the major design and operational parameters. J. Cleaner Prod. 141, 1492-1514.

Bin, Z., ShaoMin, Z., HaiWei, W., ZuLiang, D., 2008. Raman scattering and photoluminescence of Fe-doped ZnO nanocantilever arrays. Chin. Sci. Bull. 53(11), 1639-1643.

Briggs, D., 1981. Handbook of X□ray Photoelectron Spectroscopy CD Wanger, WM Riggs, LE Davis, JF Moulder and GE Muilenberg Perkin□Elmer Corp., Physical Electronics Division, Eden Prairie, Minnesota, USA, 1979. 190 pp. $195. Surf. Interface Anal. 3(4), v-v.

Chong, M.N., Jin, B., Chow, C.W., Saint, C., 2010. Recent developments in photocatalytic water treatment technology: a review. Water Res. 44(10), 2997-3027.
Chow, K.L., Man, Y.B., Tam, N.F.Y., Liang, Y., Wong, M.H., 2017. Removal of decabromodiphenyl ether (BDE-209) using a combined system involving TiO2 photocatalysis and wetland plants. J. Hazard. Mater. 322, 263-269.

Gahlout, M., Gupte, S., Gupte, A., 2013. Optimization of culture condition for enhanced decolorization and degradation of azo dye reactive violet 1 with concomitant production of ligninolytic enzymes by Ganoderma cupreum AG-1. 3 Biotech 3(2), 143-152.

Giannakis, S., Liu, S., Carratalà, A., Rtimi, S., Amiri, M.T., Bensimon, M., Pulgarin, C., 2017. Iron oxide-mediated semiconductor photocatalysis vs. heterogeneous photo-Fenton treatment of viruses in wastewater. Impact of the oxide particle size. J. Hazard. Mater. 339, 223-231.

Han, F., Kambala, V.S.R., Srinivasan, M., Rajarathnam, D., Naidu, R., 2009. Tailored titanium dioxide photocatalysts for the degradation of organic dyes in wastewater treatment: a review. Appl. Catal., A 359(1-2), 25-40.

Harifi, T., Montazer, M., 2014. Photo-, bio-, and magneto-active colored polyester fabric with hydrophobic/hydrophilic and enhanced mechanical properties through synthesis of TiO2/Fe3O4/Ag nanocomposite. Ind. Eng. Chem. Res. 53(3), 1119-1129.

Hassan, M., Wang, X., Wang, F., Wu, D., Hussain, A., Xie, B., 2017. Coupling ARB-based biological and photochemical (UV/TiO2 and UV/S2O82−) techniques to deal with sanitary landfill leachate. Waste Manage. 63, 292-298.

Hoffmann, M.R., Martin, S.T., Choi, W., Bahnemann, D.W., 1995. Environmental applications of semiconductor photocatalysis. Chem. Rev. 95(1), 69-96.

Iqbal, J., Jan, T., Ronghai, Y., Naqvi, S.H., Ahmad, I., 2014. Doping induced tailoring in the morphology, band-gap and ferromagnetic properties of biocompatible ZnO nanowires, nanorods and nanoparticles. Nano-Micro Lett. 6(3), 242-251.

Islam, M.N., Ghosh, T., Chopra, K., Acharya, H., 1996. XPS and X-ray diffraction studies of aluminum-doped zinc oxide transparent conducting films. Thin Solid Films 280(1-2), 20-25.

Jeong, H.W., Choi, S.-Y., Hong, S.H., Lim, S.K., Han, D.S., Abdel-Wahab, A., Park, H., 2014. Shape-dependent charge transfers in crystalline ZnO photocatalysts: rods versus plates. J. Phys. Chem. C 118(37), 21331-21338.

Kang, U., Park, H., 2013. Lithium ion-inserted TiO2 nanotube array photoelectrocatalysts. Appl. Catal., B 140, 233-240.

Kannangara, Y.Y., Wijesena, R., Rajapakse, R., de Silva, K.N., 2018. Heterogeneous photocatalytic degradation of toluene in static environment employing thin films of nitrogen-doped nano-titanium dioxide. Int. Nano Lett. 8(1), 31-39.

Kansal, S., Singh, M., Sud, D., 2007. Studies on photodegradation of two commercial dyes in aqueous phase using different photocatalysts. J. Hazard. Mater. 141(3), 581-590.

Karamat, S., Rawat, R., Lee, P., Tan, T., Ramanujan, R., 2014. Structural, elemental, optical and magnetic study of Fe doped ZnO and impurity phase formation. Pro. Nat. Sci-Mater. 24(2), 142-149.

Karmakar, D., Mandal, S., Kadam, R., Paulose, P., Rajarajan, A., Nath, T.K., Das, A.K., Dasgupta, I., Das, G., 2007. Ferromagnetism in Fe-doped ZnO nanocrystals: experiment and theory. Phys. Rev. B: Condens. Matter 75(14), 144404.

Katal, R., Salehi, M., Davood Abadi Farahani, M.H., Masudy-Panah, S., Ong, S.L., Hu, J., 2018. Preparation of a New Type of Black TiO2 under a Vacuum Atmosphere for Sunlight Photocatalysis. ACS Appl. Mater. Interfaces 10(41), 35316-35326.

Kaur, J., Kumar, V., Gupta, K., Bansal, S., Singhal, S., 2016. A facile strategy for the degradation of recalcitrant textile dyes using highly robust ZnO catalyst. J. Chem. Technol. Biotechnol. 91(8), 2263-2275.

Kazeminezhad, I., Sadollahkhani, A., 2016. Influence of pH on the photocatalytic activity of ZnO nanoparticles. Journal of Materials Science: Materials in Electronics 27(5), 4206-4215.

Kołodziejczak-Radzimska, A., Jesionowski, T., 2014. Zinc oxide—from synthesis to application: a review. Materials 7(4), 2833-2881.

Koper, O., Klabunde, K.J., 1997. Destructive adsorption of chlorinated hydrocarbons on ultrafine (nanoscale) particles of calcium oxide. 3. Chloroform, trichloroethene, and tetrachloroethene. Chem. Mater. 9(11), 2481-2485.

Lee, A.Y., Blakeslee, D.M., Powell, C.J., Rumble Jr, J.R., 2002. Development of the web-based NIST X-ray Photoelectron Spectroscopy (XPS) Database. Data Sci. J. 1, 1-12.

Lee, Y., Lu, Y., Park, S., Huang, M., Rhee, J., 2008. Magneto-optical characteristics of symmetric and asymmetric spin photonic crystals. J. Korean Phys. Soc. 52, S1-S4.

Li, Z., Sun, Y., Xing, J., Xing, Y., Meng, A., 2018. One step synthesis of Co/Cr-codoped ZnO nanoparticle with superb adsorption properties for various anionic organic pollutants and its regeneration. J. Hazard. Mater. 352, 204-214.

Long, L., Xue, Y., Zeng, Y., Yang, K., Lin, C., 2017. Synthesis, characterization and mechanism analysis of modified crayfish shell biochar possessed ZnO nanoparticles to remove trichloroacetic acid. J. Cleaner Prod. 166, 1244-1252.

Molinari, R., Lavorato, C., Argurio, P., 2017. Recent progress of photocatalytic membrane reactors in water treatment and in synthesis of organic compounds. A review. Catal. Today 281, 144-164.

Moulder, J., Stickle, W., Sobol, P., Bomben, K., 1992. Handbook of X-ray photoelectron spectroscopy; Chastain, J. Perkin-Elmer Corp., Eden Prairie, MN.

Mozia, S., Darowna, D., Szymański, K., Grondzewska, S., Borchert, K., Wróbel, R., Morawski, A.W., 2014. Performance of two photocatalytic membrane reactors for treatment of primary and secondary effluents. Catal. Today 236, 135-145.

Neoh, C.H., Lam, C.Y., Lim, C.K., Yahya, A., Bay, H.H., Ibrahim, Z., Noor, Z.Z., 2015. Biodecolorization of recalcitrant dye as the sole sourceof nutrition using Curvularia clavata NZ2 and decolorization ability of its crude enzymes. Environ. Sci. Pollut. Res. 22(15), 11669-11678.

Park, H., Kim, H.-i., Moon, G.-h., Choi, W., 2016. Photoinduced charge transfer processes in solar photocatalysis based on modified TiO 2. Energy Environ. Sci. 9(2), 411-433.

Park, H., Park, Y., Kim, W., Choi, W., 2013. Surface modification of TiO2 photocatalyst for environmental applications. J. Photochem. Photobiol., C 15, 1-20.

Park, Y., Kim, W., Park, H., Tachikawa, T., Majima, T., Choi, W., 2009. Carbon-doped TiO2 photocatalyst synthesized without using an external carbon precursor and the visible light activity. Appl. Catal., B 91(1-2), 355-361.

Prieto-Rodriguez, L., Miralles-Cuevas, S., Oller, I., Agüera, A., Puma, G.L., Malato, S., 2012. Treatment of emerging contaminants in wastewater treatment plants (WWTP) effluents by solar photocatalysis using low TiO2 concentrations. J. Hazard. Mater. 211, 131-137.

Rambu, A., Nica, V., Dobromir, M., 2013. Influence of Fe-doping on the optical and electrical properties of ZnO films. Superlattices Microstruct. 59, 87-96.

Sahel, K., Perol, N., Dappozze, F., Bouhent, M., Derriche, Z., Guillard, C., 2010. Photocatalytic degradation of a mixture of two anionic dyes: Procion Red MX-5B and Remazol Black 5 (RB5). J. Photochem. Photobiol., A 212(2), 107-112.

Sarkar, S., Makhal, A., Bora, T., Lakhsman, K., Singha, A., Dutta, J., Pal, S.K., 2012. Hematoporphyrin–ZnO nanohybrids: twin applications in efficient visible-light photocatalysis and dye-sensitized solar cells. ACS Appl. Mater. Interfaces 4(12), 7027-7035.

Shinde, D.R., Qureashi, I., Pawar, R.A., Pawar, R., 2015. Enhancement of photocatalytic activity of ZnO via Nd (III) doping towards the degradation of dyes under solar irradiation. J. Nanoeng. Nanomanuf. 5(3), 197-203.

Srinivasulu, T., Saritha, K., Reddy, K.R., 2017. Synthesis and characterization of Fe-doped ZnO thin films deposited by chemical spray pyrolysis. Mod. Electron. Mater. 3(2), 76-85.

Sun, Y., Chen, L., Bao, Y., Zhang, Y., Wang, J., Fu, M., Wu, J., Ye, D., 2016. The applications of morphology controlled ZnO in catalysis. Catalysts 6(12), 188.

Tabata, M., Maeda, K., Higashi, M., Lu, D., Takata, T., Abe, R., Domen, K., 2010. Modified Ta3N5 powder as a photocatalyst for O2 evolution in a two-step water splitting system with an iodate/iodide shuttle redox mediator under visible light. Langmuir 26(12), 9161-9165.

Talinungsang, N.P., Purkayastha, D.D., 2017. SnO2/TiO2 bilayer thin films exhibiting superhydrophilic properties, AIP Conference Proceedings. AIP Publishing, 1832(1): p. 080035.

Thompson, T.L., Yates, J.T., 2006. Surface science studies of the photoactivation of TiO2 new photochemical processes. Chem. Rev. 106(10), 4428-4453.
Wang, Y., Yuan, S., Liu, L., Li, P., Lan, X., Tian, Z., He, J., Yin, S., 2008. Ferromagnetism in Fe-doped ZnO bulk samples. J. Magn. Magn. Mater. 320(8), 1423-1426.

Yu, D., Wang, H., Yang, J., Niu, Z., Lu, H., Yang, Y., Cheng, L., Guo, L., 2017. Dye wastewater cleanup by graphene composite paper for tailorable supercapacitors. ACS Appl. Mater. Interfaces 9(25), 21298-21306.

Yücel, E., Yücel, Y., 2015. Optimization of zinc sulfide thin film coating process using response surface methodology. J. Mater. Sci. - Mater. Electron. 26(1), 196-203.

Zhang, W., Liu, W., Zhang, J., Zhao, H., Zhang, Y., Quan, X., Jin, Y., 2012. Characterisation of acute toxicity, genotoxicity and oxidative stress posed by textile effluent on zebrafish. J. Environ. Sci. 24(11), 2019-2027.

Zheng, L., Xu, Y., Song, Y., Wu, C., Zhang, M., Xie, Y., 2009. Nearly monodisperse CuInS2 hierarchical microarchitectures for photocatalytic H2 evolution under visible light. Inorg. Chem. 48(9), 4003-4009.

Zheng, X., Shen, Z.-P., Shi, L., Cheng, R., Yuan, D.-H., 2017. Photocatalytic Membrane Reactors (PMRs) in Water Treatment: Configurations and Influencing Factors. Catalysts 7(8), 224.

Zheng, Y., Chen, C., Zhan, Y., Lin, X., Zheng, Q., Wei, K., Zhu, J., Zhu, Y., 2007. Luminescence and photocatalytic activity of ZnO nanocrystals: correlation between structure and property. Inorg. Chem. 46(16), 6675-6682.

Kazeminezhad, I., Sadollahkhani, A., 2016. Influence of pH on the photocatalytic activity of ZnO nanoparticles. Journal of Materials Science: Materials in Electronics 27(5), 4206-4215.

Table 2. Lattice parameters of Fe^{3+}@ZnO samples.

S. No.	Sample doping	Peak position (2θ)	FWHM	Crystallite size(nm)	Crystal constants
1	Fe^{3+}@ZnO 0.0wt%	36.321	0.320	28.35	a= 3.25340 Å c= 5.20730 Å
2	Fe^{3+}@ZnO 0.2wt%	36.314	0.354	26.60	a= 3.25322 Å c= 5.20719 Å
3	Fe^{3+}@ZnO 0.4wt%	36.310	0.362	23.05	a= 3.24950 Å c= 5.20710 Å
4	Fe^{3+}@ZnO 0.6wt%	36.291	0.383	21.34	a= 3.24937 Å c= 5.20470 Å
5	Fe^{3+}@ZnO 0.8wt%	36.276	0.389	21.88	a= 3.24931 Å c= 5.20571 Å
6	Fe^{3+}@ZnO 1.0wt%	36.145	0.319	29.30	a= 3.24937 Å c= 5.19910 Å

NOTE: Place this table at page 7 of main manuscript

Highlights

- Development of visible light driven photocatalytic membrane reactors
- Doping of ZnO with Fe^{+3} to reduce bandgap for solar light harvesting
- Degradation of dyes to treat industrial effluent

Declaration of interests

☒ The authors declare that they have no known competing financial interests or personal relationships that could have appeared to influence the work reported in this paper.

☐The authors declare the following financial interests/personal relationships which may be considered as potential competing interests: